

# Gas metallicity distributions in SDSS-IV MaNGA galaxies: what drives gradients and local trends?

N. Boardman<sup>1\*</sup>, V. Wild<sup>1</sup>, T. Heckman<sup>2</sup>, S. F. Sanchez<sup>3</sup>, R. Riffel<sup>4,5</sup>, R. A. Riffel<sup>5,6</sup>, G. Zasowski<sup>7</sup>

<sup>1</sup>*School of Physics and Astronomy, University of St Andrews, North Haugh, St Andrews KY16 9SS, UK*

<sup>2</sup>*The William H. Miller III Department of Physics & Astronomy, Johns Hopkins University, Baltimore, MD 21218, United States*

<sup>3</sup>*Universidad Nacional Autónoma de México, Instituto de Astronomía, A.P. 70-264, 04510, Mexico, D.F., Mexico*

<sup>4</sup>*Departamento de Astronomia, Instituto de Física, Universidade Federal do Rio Grande do Sul, CP 15051, 91501-970, Porto Alegre, RS, Brazil*

<sup>5</sup>*Laboratório Interinstitucional de e-Astronomia - LIneA, Rua Gal. José Cristino 77, Rio de Janeiro, RJ - 20921-400, Brazil*

<sup>6</sup>*Departamento de Física, CCNE, Universidade Federal de Santa Maria, 97105-900, Santa Maria, RS, Brazil*

<sup>7</sup>*Department of Physics & Astronomy, University of Utah, Salt Lake City, UT, 84112, USA*

Accepted X. Received X; in original form X

## ABSTRACT

The gas metallicity distributions across individual galaxies and across galaxy samples can teach us much about how galaxies evolve. Massive galaxies typically possess negative metallicity gradients, and mass and metallicity are tightly correlated on local scales over wide range of galaxy masses; however, the precise origins of such trends remain elusive. Here, we employ data from SDSS-IV MaNGA to explore how gas metallicity depends on local stellar mass density and on galactocentric radius within individual galaxies. We also consider how the strengths of these dependencies vary across the galaxy mass-size plane. We find that radius is more predictive of local metallicity than stellar mass density in extended lower mass galaxies, while we find density and radius to be almost equally predictive in higher-mass and more compact galaxies. Consistent with previous work, we find a mild connection between metallicity gradients and large-scale environment; however, this is insufficient to explain variations in gas metallicity behaviour across the mass-size plane. We argue our results to be consistent with a scenario in which extended galaxies have experienced smooth gas accretion histories, producing negative metallicity gradients over time. We further argue that more compact and more massive systems have experienced increased merging activity that disrupts this process, leading to flatter metallicity gradients and more dominant density-metallicity correlations within individual galaxies.

**Key words:** galaxies: ISM – galaxies: structure – galaxies: general – ISM: general – galaxies: statistics – ISM: abundances

## 1 INTRODUCTION

Gas-phase chemical abundances in galaxies are products of a range of physical processes; thus, these abundances can teach us much about how galaxies form and evolve. Modern integral-field unit (IFU) datasets – including CALIFA (Sánchez et al. 2012a), SAMI (Croom et al. 2012), and MaNGA (Bundy et al. 2015) – provide spatial distributions of abundances across large numbers of galaxies and have led to a range of advances over the preceding decade.

Notably, the majority of massive galaxies possess negative gas metallicity gradients. Sánchez et al. (2014), for instance, report a characteristic slope of  $-0.1$  dex per disc effective radius in their sample of CALIFA galaxies (see also Sánchez et al. 2012b), and Sánchez-Menguiano et al. (2018) report a similar slope in their MUSE galaxy sample. Gas metallicity gradients have been reported from observations to correlate

with a range of other galaxy properties including stellar mass (Belfiore et al. 2017; Mingozzi et al. 2020; Schaefer et al. 2020; Franchetto et al. 2021), size (Carton et al. 2018), gas fraction (Franchetto et al. 2021), bulge-to-total (B/T) ratio (Moran et al. 2012), and environment (Lian et al. 2019; Franchetto et al. 2021). Boardman et al. (2021) report a tight trend in gradients across the mass-size plane for MaNGA galaxies, wherein more extended galaxies display more strongly negative gradients at a given stellar mass; this is similar to what was reported for stellar metallicity gradients by Li et al. (2018), and is found in Boardman et al. (2021) to be significantly tighter than gradient trends with mass or size individually. Such a result is also analogous to the apparent complex connection between metallicity gradient, mass and morphology (Sánchez et al. 2021), due to the tight trend between galaxy size and morphology at a given stellar mass (e.g. Fernández Lorenzo et al. 2013).

A number of local  $\sim$ kpc-scale relations involving gas metallicity have also been reported in the literature. An exam-

\* E-mail: nfb@st-andrews.ac.uk

ple of this is the resolved mass-metallicity relation (rMZR) between gas metallicity and stellar mass surface density  $\Sigma_*$  (e.g. Rosales-Ortega et al. 2012; Sánchez et al. 2013; Barrera-Ballesteros et al. 2016), which can be understood as reflecting a tight interplay between gas metallicities and local conditions (e.g. Barrera-Ballesteros et al. 2018), though an additional metallicity dependence on stellar mass is also apparent for lower-mass galaxies in particular (e.g., Barrera-Ballesteros et al. 2016; Gao et al. 2018; Hwang et al. 2019). Barrera-Ballesteros et al. (2016) argue that the rMZR alone is sufficient to reproduce metallicity gradients over stellar masses between  $10^9$  and  $10^{11} M_\odot$ , while Boardman et al. (2022, hereafter B22) find local relations – involving metallicity,  $\Sigma_*$ , stellar mass  $M_*$ , stellar age and the D4000 index (Bruzual 1983) – to predict gradient trends across the mass-size plane qualitatively similar to what is observed. Thus, gas metallicity gradients can potentially be understood as arising from local conditions across a galaxy, with inside-out formation naturally producing negative metallicity gradients in star-forming galaxies (e.g. Franchetto et al. 2021).

Chemical evolution models can provide us with additional insight into gas metallicities. In the simple “closed-box” model (Schmidt 1963), the interstellar medium (ISM) is enriched by successive stellar generations and the gas metallicity depends solely on the local gas fraction, with higher metallicities associated with lower gas fractions. More complex models also consider the effects of inflow and outflow, at which point the local escape velocity also becomes relevant (e.g. Lilly et al. 2013; Zhu et al. 2017). Recent observational studies have generally favoured both gas fraction and escape velocity as being important in shaping the gas metallicity (Moran et al. 2012; Carton et al. 2015; Barrera-Ballesteros et al. 2018). The rMZR provides a tighter correlation overall than do gas fraction or escape velocity, however, which could potentially be due to  $\Sigma_*$  encoding information on both of these parameters (Barrera-Ballesteros et al. 2018).

Typically, studies of the rMZR along with other local relations consider large samples of star-forming regions observed over many separate galaxies. However, further information can be gained by considering local trends within individual galaxies. An example of this can be seen in Sánchez-Menguiano et al. (2019), who investigate residual trends between gas metallicity and star-formation rate within individual MaNGA galaxies. In particular, the opportunity exists to determine whether the rMZR is the most fundamental local relation within individual systems.

Here, we employ SDSS MaNGA data to assess the strength of the correlation between metallicity and  $\Sigma_*$  in individual galaxies, which we then compare to the strength of correlation between metallicity and galactocentric radius. Our direct use of radius is motivated by the steep gas metallicity gradients measured in extended star-forming MaNGA galaxies, along with the radial dependencies in both gas mass fractions (e.g. Carton et al. 2015) and escape velocities within galaxies. We consider the gas metallicity as given by the oxygen abundance,  $12 + \log(\text{O}/\text{H})$ . We then investigate whether our results could be explained by variations in galaxies’ environments, motivated primarily by the work of Franchetto et al. (2021).

This article is structured as follows. We present our sample and explain relevant parameters in § 2. We present our results in § 3 and discuss our findings in § 4, before summarising

and concluding in § 5. Throughout this work, we assume a Kroupa IMF (Kroupa 2001; Kroupa & Weidner 2003) and we adopt the following standard  $\Lambda$  Cold Dark Matter cosmology:  $H_0 = 71$  km/s/Mpc,  $\Omega_M = 0.27$ ,  $\Omega_\Lambda = 0.73$ .

## 2 SAMPLE AND DATA

We employ integral-field spectroscopic data from the SDSS-IV MaNGA survey. The MaNGA survey observed galaxies with the BOSS spectrographs (Smee et al. 2013) on the 2.5 meter telescope at Apache point observatory (Gunn et al. 2006). The MaNGA galaxy sample covers redshifts over the approximate range of 0.01 to 0.15, and was selected to possess a roughly flat logarithmic mass distribution (Yan et al. 2016b; Wake et al. 2017). The MaNGA IFUs consist of bundles of 19-127 optical fibres with  $2''$  diameters (Law et al. 2016). The IFUs employ hexagonal fibre configurations, and galaxies are observed with three-point dither patterns to fully sample the field of view (Drory et al. 2015; Law et al. 2015). The MaNGA data reduction pipeline (DRP; Law et al. 2016; Yan et al. 2016a) reduces the data, producing  $0.5'' \times 0.5''$  spaxel datacubes with a median PSF full-width at half-maximum (FWHM) of roughly  $2.5''$  (Law et al. 2016). The MaNGA data analysis pipeline (DAP; Belfiore et al. 2019a; Westfall et al. 2019) then computes various mapped quantities relating to stellar and gaseous galaxy components. MaNGA data and derived quantities are accessible through the SDSS Science Archive Server<sup>1</sup>, and can also be accessed through the Marvin<sup>2</sup> interface (Cherinka et al. 2019). The reduced spectra have a resolution of  $R \simeq 2000$  and cover a wavelength range of 3600–10000Å. The full MaNGA galaxy sample consists of more than 10000 galaxies as of SDSS DR17 (Abdurro’uf et al. 2022); however, only a subset of these will be suitable for studying gas metallicities and gas metallicity gradients.

We selected a sample of MaNGA galaxies and spaxels in almost exactly the same manner as in B22, employing values from the DAP and from Pipe3D (Sánchez et al. 2016a,b, 2018). Our one difference from B22 is that we employ the DR17 versions of Pipe3D and the DAP. We therefore refer the reader to B22 for a full description of the sample selection, though we also summarise it here. In brief, we begin by selecting MaNGA galaxies from the MPL-10 data release (which contains  $\sim 9000$  galaxies) with NASA-Sloan-Atlas (NSA; Blanton et al. 2011) elliptical Petrosian axis ratios (b/a) of at least 0.6 to avoid edge-on cases, and we cross-match with the 2X version of the GALEX-SDSS-WISE Legacy catalog (GSWLC; Salim et al. 2016, 2018) to obtain stellar masses. We identify star-forming spaxels with galactocentric radii between  $0.5 R_e$  and  $2 R_e$  using the BPT-NII diagnostic diagram (Baldwin et al. 1981) and by requiring a minimum  $\text{H}\alpha$  equivalent width of 10, and we require a minimum S/N of 3 for the following emission features:  $\text{H}\alpha$ ,  $\text{H}\beta$ ,  $[\text{OIII}]\lambda 5007$ ,  $[\text{NII}]\lambda 6583$  and  $[\text{OII}]\lambda 3737, 3729$ . We further restrict to galaxies with at least 20 star-forming spaxels. We employ Pipe3d  $\Sigma_*$  values along with the associated uncertainties. As in past works (e.g. Barrera-Ballesteros et al. 2016; Boardman et al. 2022), we multiply observed  $\Sigma_*$  values (along with the errors) by b/a to correct for the effects of inclination.

<sup>1</sup> <https://data.sdss.org/sas/>

<sup>2</sup> <https://www.sdss.org/dr17/manga/marvin/>

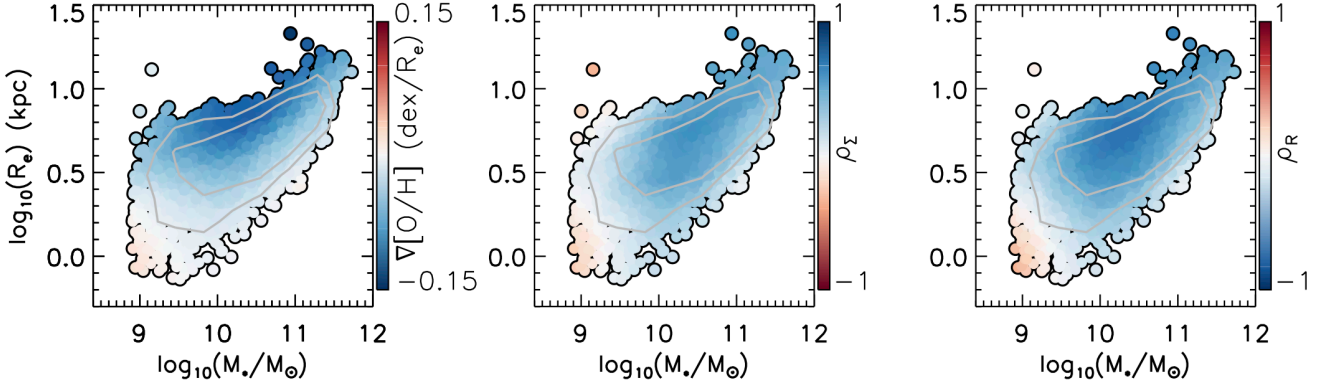


**Figure 1.** Effective radius, plotted against galaxy stellar mass, with data points coloured by the radial gas metallicity gradients (left) and by the Spearman correlation coefficients between  $\Sigma_*$  and metallicity (middle) and between radius and metallicity (right). We apply LOESS smoothing in all panels. The middle panel uses a reversed colour scale; thus, blue regions correspond to negative gradients, positive  $\Sigma_*$ -metallicity correlations and negative radius-metallicity correlations. The contours enclose  $\sim 50\%$  and  $\sim 80\%$  of galaxies.

We then calculate gas metallicity maps for each sample galaxy using DAP emission line fluxes with the Marino et al. (2013, hereafter M13) calibrator. The M13 calibrator estimates gas metallicity at  $12 + \log(\text{O}/\text{H}) = 8.533 - 0.214 \text{ O3N2}$ , where O3N2 is given as

$$\text{O3N2} = \log \left( \frac{[\text{OIII}]\lambda 5007}{\text{H}\beta} \times \frac{\text{H}\alpha}{[\text{NII}]\lambda 6583} \right) \quad (1)$$

O3N2 calibrators have the advantage of being essentially unaffected by dust extinction. However, these calibrators implicitly assume a fixed N/O–O/H relation, which can bias metallicity gradient measurements in certain cases. Thus, as in B22, we present in Appendix A results from the R2 calibrator described in Pilyugin & Grebel (2016), though we will focus on the M13 calibrator in the main paper text. As explored further in Appendix A, we obtain similar outcomes from both calibrators.

B22 generated ‘model’ metallicities from local relations, which they used to predict gas metallicity gradients for comparisons with observed gradients. The first of these model sets, termed ‘base models’ in B22, constructed metallicity predictions using the three-way relation between  $M_*$ ,  $\Sigma_*$  and  $12 + \log(\text{O}/\text{H})$  (e.g. Gao et al. 2018). For the second model set, termed ‘star formation history models’ (hereafter ‘SFH models’, B22 corrected the base models for the two-dimensional residual dependence on D4000 (Bruzual 1983) and on light-weighted pipe3d stellar age. We construct these two model sets in the exact same manner as described in B22. We remove spaxels in sparsely-sampled regions of the parameter space at this stage, and we remove galaxies (along with associated spaxels) that are left with fewer than 20 star-forming spaxels afterwards. Following some additional cuts as described in B22, we obtain a final sample consisting of 2127 galaxies containing 860214 individual star-forming spaxels.

The resulting sample is dominated by galaxies with significant ongoing star-formation: 2027 (95%) of the galaxies possess GSWLC-2X specific star formation rates (sSFRs) above  $10^{-11} \text{ yr}^{-1}$ , while only 15 (0.7%) possess sSFRs below  $10^{-11.5} \text{ yr}^{-1}$ . We calculate gas metallicity gradients for

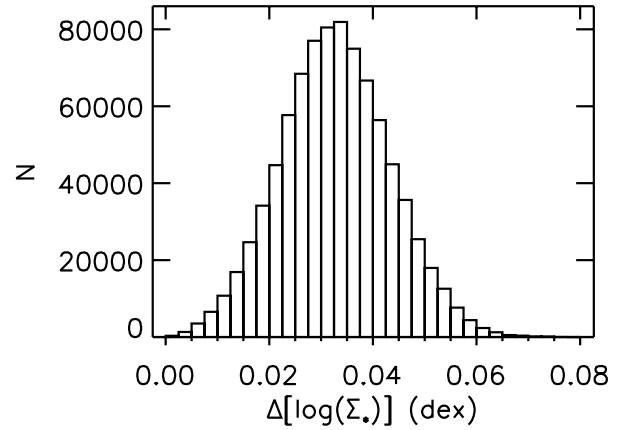


**Figure 2.** Histogram of errors in  $\log(\Sigma_*)$ .

each galaxy in units of  $\text{dex}/R_e$ , as described in B22, where  $R_e$  is the elliptical Petrosian half-light radius from the NSA catalog.

We also obtain from Duckworth et al. (2019) a set of environmental parameters calculated for MaNGA galaxies. The first two of these are  $\rho_{3\text{Mpc}}$  and  $\rho_{9\text{Mpc}}$ , which denote galaxy environment densities smoothed with a Gaussian kernel over local scales (3 Mpc) and larger scales (9 Mpc). In addition to these, we consider galaxies’  $D_{\text{skel}}$  and  $D_{\text{node}}$  parameters, which denote the distances to cosmic web nodes and filaments respectively. As in Duckworth et al. (2019), we normalise  $D_{\text{skel}}$  and  $D_{\text{node}}$  by the mean inter-galaxy separation at a given redshift,  $\langle D_z \rangle = n(z)^{-1/3}$  where  $n(z)$  is the co-moving number density; we calculate the number density as a function of redshift using the Tempel et al. (2014) spectroscopic catalog of SDSS DR10 galaxies.

### 3 RESULTS

#### 3.1 Correlations of density and radius with gas metallicity

We begin by considering the strength of the correlations of  $\Sigma_*$  and normalised galactocentric radius  $R/R_e$  with gas-phase metallicity, for spaxels in each sample galaxy separately. We parametrize this strength using the Spearman rank correlation coefficient  $\rho$ , computed from the IDL `R_CORRELATE` procedure for each galaxy in turn; we denote the coefficient between gas metallicity and  $\Sigma_*$  as  $\rho_\Sigma$ , while for gas metallicity and radius we use  $\rho_R$ .

In Figure 1, we plot these coefficients across the mass-size plane along with the radial gas metallicity gradients ( $\nabla[O/H]$ ) from B22. We employ locally-weighted regression smoothing (LOESS; Cleveland & Devlin 1988) as implemented in IDL<sup>3</sup> when showing these figures, to more cleanly show the overall mass-size trend. We compute the LOESS-smoothed value for each data point using the closest 20% of data points with the *rescale* keyword applied. We compute errors from the scatter in neighbouring points for the purpose of the smoothing calculation.

It is apparent from Figure 1 – unsurprisingly so – that the coefficients trend similarly to the gradients across the plane, with the strongest correlations seen in more massive extended galaxies for both  $\Sigma_*$  and  $R$ . We further explore the connection between the gradients and correlation coefficients in Appendix B.

From Figure 1, the absolute values of  $\rho_R$  are typically as high or higher than  $\rho_\Sigma$ . However, it is not truly fair to compare  $\rho_\Sigma$  and  $\rho_R$  directly, since  $\Sigma_*$  possesses non-negligible measurement errors compared to  $R$ . Thus, before comparing these two parameters further, we perturb the radii of spaxels to approximately match the effect of the  $\Sigma_*$  errors.

We perturb spaxels’  $R/R_e$  as follows. The error in  $\Sigma_*$  is typically well below 0.1 dex, as shown in Figure 2; thus, we adopt 0.1 dex as a conservative estimate for the level of scatter in  $\Sigma_*$  due to measurement/fitting uncertainties. We then apply a Gaussian scatter to spaxels’  $\log(R/R_e)$  of  $\Delta_R = 0.1\text{dex} \times \sigma_{\log(r)}/\sigma_{\log(\Sigma)}$ , where  $\sigma_{\log(r)}$  and  $\sigma_{\log(\Sigma)}$  denote the dispersions<sup>4</sup> in  $\log(R/R_e)$  and  $\log(\Sigma_*)$  over the full spaxel sample. We obtain  $\sigma_{\log(r)} = 0.149\text{dex}$  and  $\sigma_{\log(\Sigma)} = 0.409\text{dex}$ , and we hence adopt  $\Delta_R = 0.036\text{dex}$  when perturbing spaxel radii. We calculate Spearman correlation coefficients between gas metallicity and the perturbed radii, and we denote these coefficients as  $\rho_{R,\text{perturbed}}$ .

In Figure 3, we plot across the mass-size plane the difference between  $|\rho_\Sigma|$  and  $|\rho_R|$  along with the difference between  $|\rho_\Sigma|$  and  $|\rho_{R,\text{perturbed}}|$ , with LOESS smoothing applied. We see a clear trend in the two  $\rho$  values: spaxels in extended galaxies with low-to-intermediate masses have metallicities more closely correlated with  $R$ , while  $\Sigma_*$  and  $R$  are almost equally predictive of the metallicity in higher-mass and more compact galaxies. We also find only mild differences in our results from using  $\rho_R$  or  $\rho_{R,\text{perturbed}}$ ; thus, the choice of  $\rho_R$  or  $\rho_{R,\text{perturbed}}$  does not significantly affect the final outcome.

<sup>3</sup> available from <http://www-astro.physics.ox.ac.uk/~mxc/software/>

<sup>4</sup> These dispersions and all subsequent dispersions are calculated using the `ROBUST_SIGMA` IDL procedure, available at [https://idlastro.gsfc.nasa.gov/ftp/pro/robust/robust\\_sigma.pro](https://idlastro.gsfc.nasa.gov/ftp/pro/robust/robust_sigma.pro)

By construction, the B22 base models cannot predict the behaviour observed in Figure 3, due to the predicted metallicity depending entirely on  $\Sigma_*$  within any given galaxy. However, the B22 SFH models depend also on D4000 and on stellar age, and so are worth considering further. We present across the mass-size plane the resulting values of  $\nabla[O/H]$ ,  $\rho_\Sigma$  and  $\rho_R$  in Figure 4, and we present the corresponding values of  $|\rho_\Sigma| - |\rho_R|$  and  $|\rho_\Sigma| - |\rho_{R,\text{perturbed}}|$  in Figure 5. We find that the SFH models likewise do not predict the observed metallicity behaviour in these regards, with  $|\rho_\Sigma|$  greater than  $|\rho_{R,\text{perturbed}}|$  over almost the whole mass-size plane once smoothing is applied. From this, we argue that radius-metallicity trends are *not* simply a consequence of the local relations covered by the B22 models.

#### 3.2 Gas metallicity as a 2D function of density and radius.

To further assess how spaxel gas metallicity varies with both  $\Sigma_*$  and  $R$ , we split our galaxy sample into subsamples based on their positions in the mass-size plane, and we then consider all spaxels within a given subsample together. Our procedure for selecting the subsamples is the same as in B22: we split the sample in stellar mass so as to encompass 1/3 of the sample apiece, and then further split the sample using the median mass-size relation calculated over a series of mass bin. We demonstrate this process in Figure 6. We deem galaxies “extended” or “compact” based on whether they lie above or below the median mass-size relation, and we deem galaxies “low-mass”, “mid-mass” or “high-mass” depending on the mass bins they fall in.

In Figure 7 we plot the spaxel gas metallicities as a combined function of  $\Sigma_*$  and  $R/R_e$  for each of the six mass-size subsamples. Here, we calculate the mean metallicity in bins of  $\Sigma_*$  and  $R/R_e$ , with all shown bins containing at least 50 spaxels. This is conceptually similar to Figure 10 of Neumann et al. (2021), which presents Firefly stellar metallicities in terms of  $\Sigma_*$  and  $R/R_e$  for galaxy subsamples split simultaneously by mass and morphology. In general, simultaneous splits by mass and morphology (and/or by mass and size) are a common way to explore galaxy samples in the literature (e.g. García-Benito et al. 2017; Sánchez 2020; Sánchez et al. 2021), and allow for additional insight compared to splitting by any one property alone. We see in Figure 7 that spaxel gas metallicities trend with both  $\Sigma_*$  and radius, and that the shape of these trends is not consistent between different mass-size bins. Metallicity trends mainly with density in low-mass compact galaxies, for instance, while at higher masses the metallicity both rises with density and falls with radius.

Our findings here possess some differences to what Neumann et al. (2021) report for stellar metallicities. In general, Neumann et al. (2021) find stellar metallicity to trend chiefly with  $\Sigma_*$  for most mass-morphology bins. For low-to-intermediate mass galaxies and for massive spirals, Neumann et al. (2021) then find stellar metallicity to rise with radius at fixed  $\Sigma_*$ . Neumann et al. (2021) argue this to require a metallicity driver in addition to  $\Sigma_*$ , with the driver serving either to raise metallicity in galaxies’ outer parts or else to dilute it in galaxies’ inner regions. By contrast, we find that gas metallicity typically falls with radius at fixed  $\Sigma_*$ , though we also find metallicity to rise with  $\Sigma_*$  at fixed radius; the only exception here is our low-mass compact galaxy subsam-

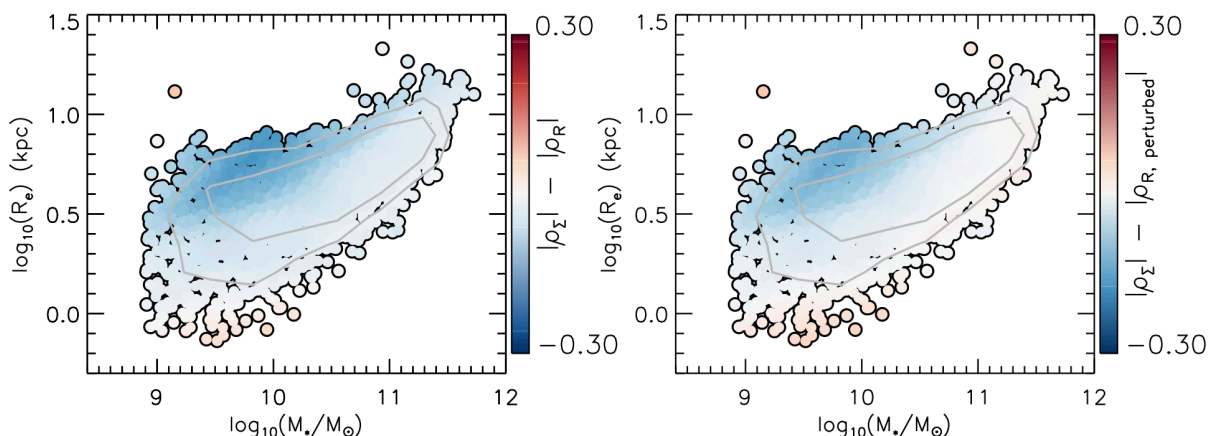


**Figure 3.** Difference in magnitudes of the Spearman correlation coefficient between gas metallicity and stellar density,  $|\rho_\Sigma|$ , and the coefficient between gas metallicity and galactocentric radius before ( $|\rho_R|$ ; left panel) and after ( $|\rho_{R, \text{perturbed}}|$ ; right panel) perturbing spaxel radii. Each datapoint represents one galaxy, and LOESS smoothing is applied; blue regions indicate where metallicity is more strongly correlated with radius, while red regions indicate a stronger correlation with density. The contours enclose  $\sim 50\%$  and  $\sim 80\%$  of galaxies.

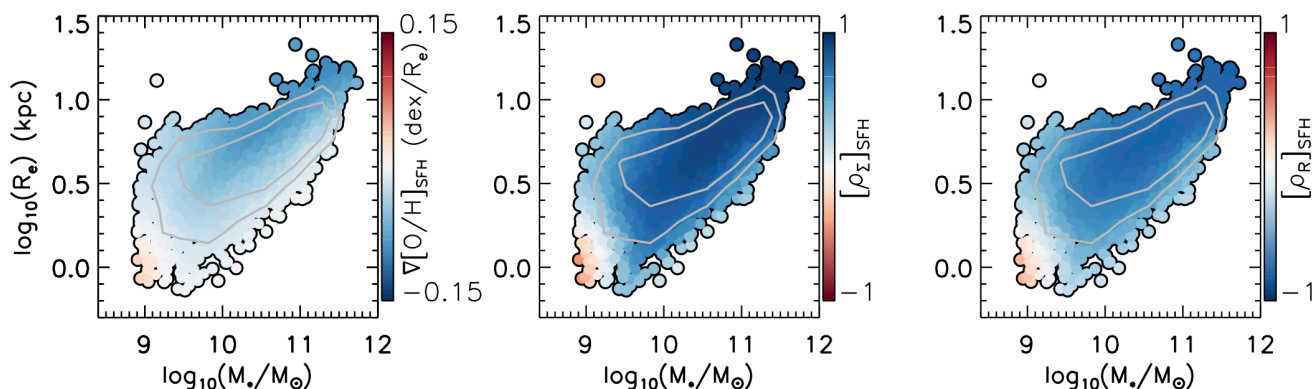


**Figure 4.** Effective radius, plotted against galaxy stellar mass, with data points coloured by the B22 ‘SFH model’ metallicity gradients (left) and by the Spearman correlation coefficients between  $\Sigma_*$  and model metallicity ( $[\rho_\Sigma]_{\text{SFH}}$ , middle) and between radius and model metallicity ( $[\rho_R]_{\text{SFH}}$ , right). We apply LOESS smoothing in all panels, and the middle panel uses a reversed colour scale. The contours enclose  $\sim 50\%$  and  $\sim 80\%$  of galaxies. We find that the SFH models do *not* reproduce the trends shown in Figures 1 and 2 for observed gas metallicities: while individual parameters behave similarly across the mass-size plane, we find local metallicities to be correlated more strongly with stellar density than with radius in most cases.

ple, which behaves similarly to what Neumann et al. (2021) report for stellar metallicities.

### 3.3 Connection with environment

From past work, the connection between gas metallicity gradients and galaxy environment appears to be small but non-negligible. Few differences are found in the gradients of satellite and central galaxies. Lian et al. (2019) only find a significant effect for satellite galaxies with  $M_* < 10^{9.7} M_\odot$ , for instance, for which denser environments are associated with flatter gradients. Schaefer et al. (2019) likewise only detect mild gradient differences between galaxies with satellite/central classi-

fications, with those differences depending on the chosen gas metallicity calibrator. On the other hand, cluster environments have been found to be associated with flatter gradients than are field environment at a given mass, in observations (Franchetto et al. 2021) as well as in simulations (Lara-López et al. 2022). Denser environments have also been reported to be associated with smaller disc galaxy sizes, particularly at lower stellar masses (e.g. Cebrián & Trujillo 2014; Kuchner et al. 2017). Thus, it is worthwhile to consider whether our gas metallicity results can be explained – at least in part – by variations in galaxies’ environments.

We now cross-match our sample with the Duckworth et al. (2019) catalog, in order to assess the importance of environ-

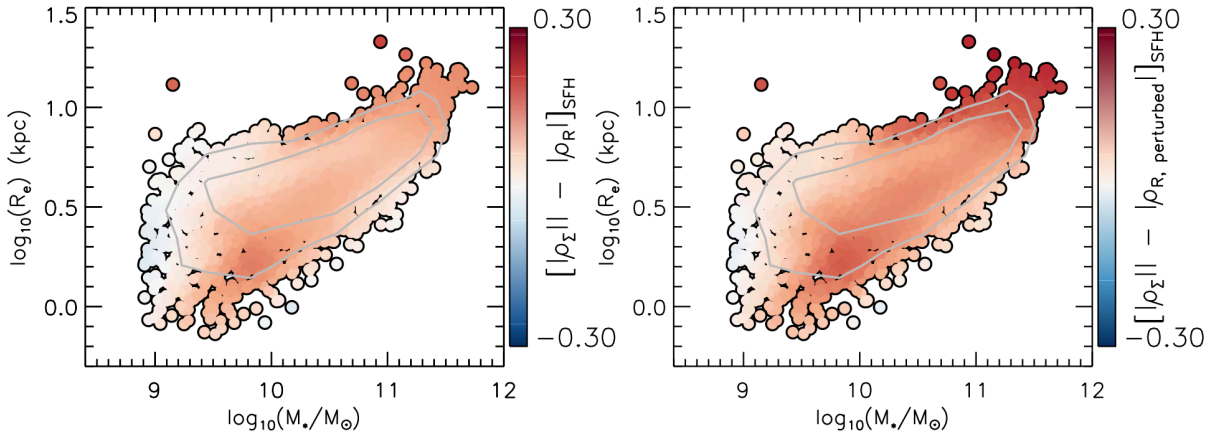


**Figure 5.** Difference in magnitudes of the Spearman correlation coefficient between SFH model gas metallicity and stellar density and the coefficient between model gas metallicity and galactocentric radius, before (left panel) and after (right panel) perturbing spaxel radii. The contours enclose  $\sim 50\%$  and  $\sim 80\%$  of galaxies. We further demonstrate here that the B22 SFH models do not predict the behaviour of observed metallicities shown in Figure 3.

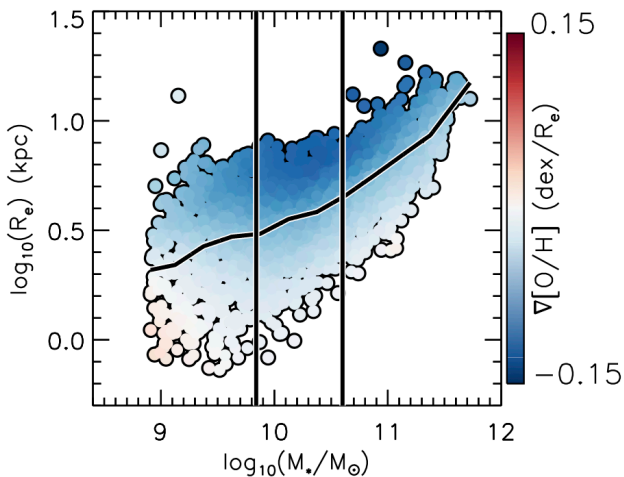


**Figure 6.** Same as the left window of Figure 1, but with the positions of our six mass-size bins overlaid. We split the galaxy sample into six subsamples accordingly, and consider these subsamples over the remainder of Section 4.2

ment for understanding our results reported up to now. We obtain environment measures for 1726 galaxies (81.1% of our sample), and we analyse only these galaxies over the remainder of this subsection. This reduction in sample size is due to Duckworth et al. (2019) employing an earlier MaNGA data-release (MPL-6) that contains fewer galaxies than MPL-10.

In Figure 8, we present the four environment quantities described in Section 2 across the mass-size plane, with LOESS smoothing applied. We see that all four quantities primarily trend with mass, such that higher mass star-forming galaxies are associated with lower environmental densities and greater distances from cosmic web features; this is different from the trends involving metallicity gradients, in which size is found

to be a significant factor. As such, we argue that environment variations are *not* sufficient to explain the variation in metallicity gradients across the mass-size plane. The finding of a mass-environment connection, we note, is likely a consequence of our selected sample: the sample consists only of star-forming galaxies by design, with the most massive star-forming galaxies then being more likely to avoid quenching by residing in less dense environments.

We probe for a connection between mass and environment in the following manner. We calculate the 10th and 90th percentiles of environment measures in bins of stellar mass; for each bin, we compute the median and dispersion of the gas metallicity gradient for all galaxies below the 10th percentile and above the 90th percentile separately. This results in eight sets of median and dispersion values for a given mass bin. We then plot the resulting values as a function of mass in Figure 9, along with showing the full environment sample. This is conceptually similar to Franchetto et al. (2021), who consider field and cluster galaxies’ gas metallicity gradients as a function of stellar mass.

It is evident from Figure 9 that galaxies in dense and sparse environments have gradients that depend differently on mass, with sparser environments – that is, larger values of  $\rho_{3Mpc}$  and  $\rho_{9Mpc}$  and/or smaller values of  $D_{skel}/\langle D_z \rangle$  and  $D_{skel}/\langle D_z \rangle$  – associated with a slightly stronger mass-gradient dependencies; this suggests that environment is a factor in gas metallicity gradients’ scatter at a given  $M_*$ , regardless of how environment is quantified.

To summarise, we detect a mild connection between the metallicity properties of star-forming galaxies and those galaxies’ large-scale environments. We find dense galaxy environments to be associated with slightly flatter metallicity gradients overall, consistent with the findings of Franchetto et al. (2021); thus, we find that environment is indeed relevant to the evolution of gas metallicity gradients. However, we find environment measures in our sample to trend primarily with mass, as opposed to trending with both mass and size. Thus, environment variations are *not* sufficient to ex-

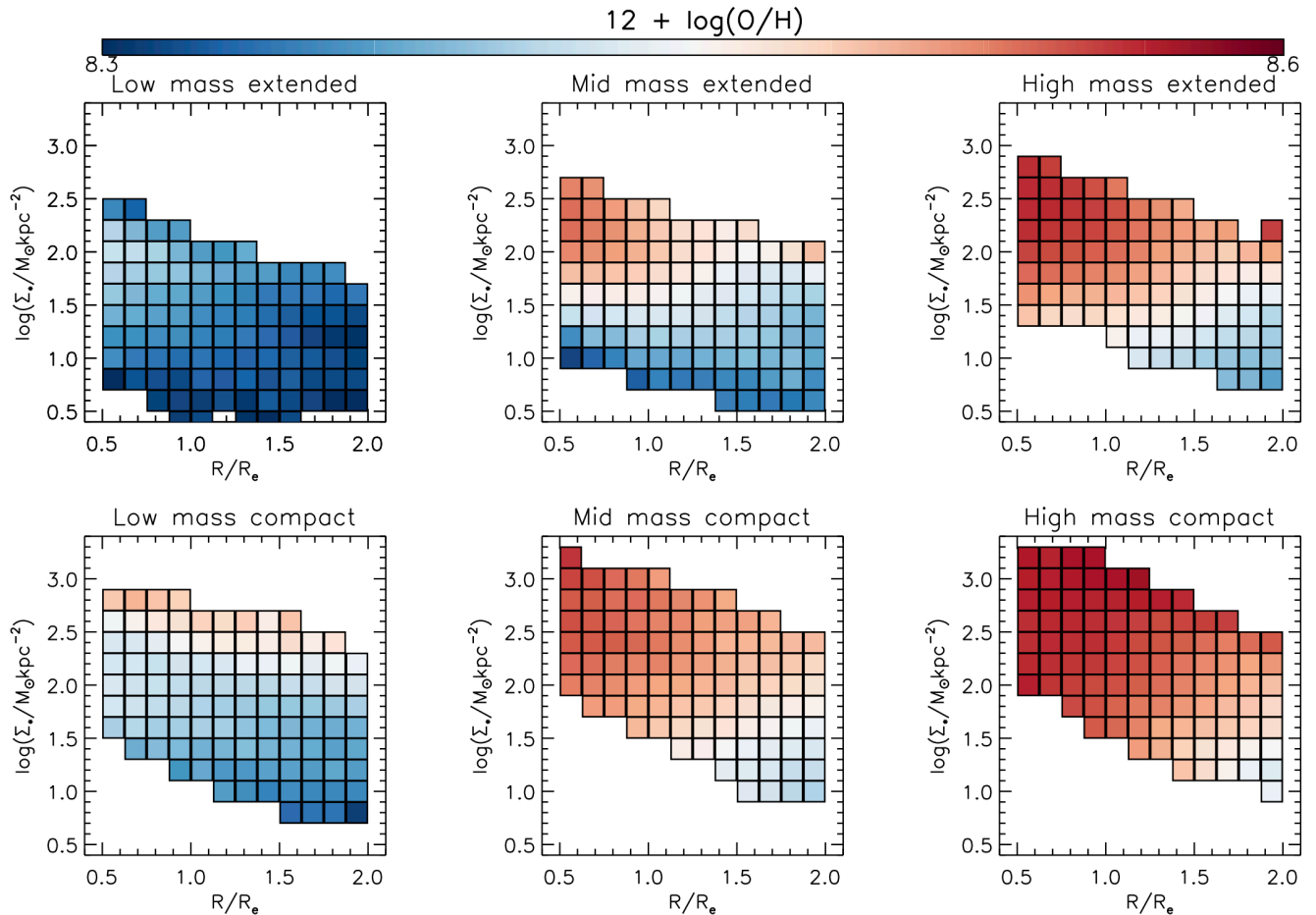


**Figure 7.** Mean observed spaxel gas metallicity in bins of stellar density and radius, for the six mass-size subsamples. Each bin encompasses a minimum of 50 spaxels. We find gas metallicity to vary with both  $\Sigma_*$  and  $R/R_e$ , with the precise behaviour differing significantly across different mass-size bins.

plain the behaviour of galaxies’ gas metallicity profiles across the mass-size plane.

#### 4 DISCUSSION

In the previous section, we employed MaNGA data to assess how metallicity connects with  $\Sigma_*$  and galactocentric radius on local ( $\sim 1$  kpc) scales. Using the Spearman correlation coefficient, we found gas metallicity to be correlated more strongly with radius than with  $\Sigma_*$  in lower-mass extended galaxies, while we found gas metallicity correlate roughly as strongly with  $\Sigma_*$  and with radius in more massive compact galaxies. We also considered spaxel metallicities as a combined function of radius and  $\Sigma_*$ , finding complex two-dimensional trends that vary with both galaxy mass and galaxy size; these trends differ somewhat from what has previously been reported for stellar metallicities (Neumann et al. 2021). Finally, we found that large-scale environment variations are *not* sufficient to explain our main findings, though we do find mild differences in gas metallicity gradients for low-density and high-density galaxy environments.

Our results for lower-mass extended galaxies imply that position within the galaxy, and *not*  $\Sigma_*$ , is the primary decider of

gas metallicity within these systems. This suggests that the rMZR computed across large spaxel samples is *not* sufficient to fully capture the metallicity behaviour in these particular galaxies. More complex local relations, such as those explored in B22, are likewise unable to predict this particular finding. The apparent importance of radius can potentially be explained as a result of the tight radial dependencies both on gas fraction (which increases with radius; e.g. Carton et al. 2015) and on escape velocity (which decreases with radius; e.g. Barrera-Ballesteros et al. 2018), both of which influence gas metallicity evolution in chemical evolution models (e.g. Lilly et al. 2013; Zhu et al. 2017) while possessing far larger uncertainties than the radius itself. In this picture, the outer parts of galaxies evolve slower (and hence take longer to use their gas supply) and receive more inflowing metal-poor gas while also being more susceptible to metal outflows, producing negative metallicity gradient as a consequence of both points.

The above picture does not explicitly consider radial flows. Recent simulations support a view in which gas primarily accretes onto the plane of a galaxy’s disc and then gradually migrates towards a galaxies’ centre (e.g. Trapp et al. 2022). Such a picture forms the basis of the ‘modified accretion disc’

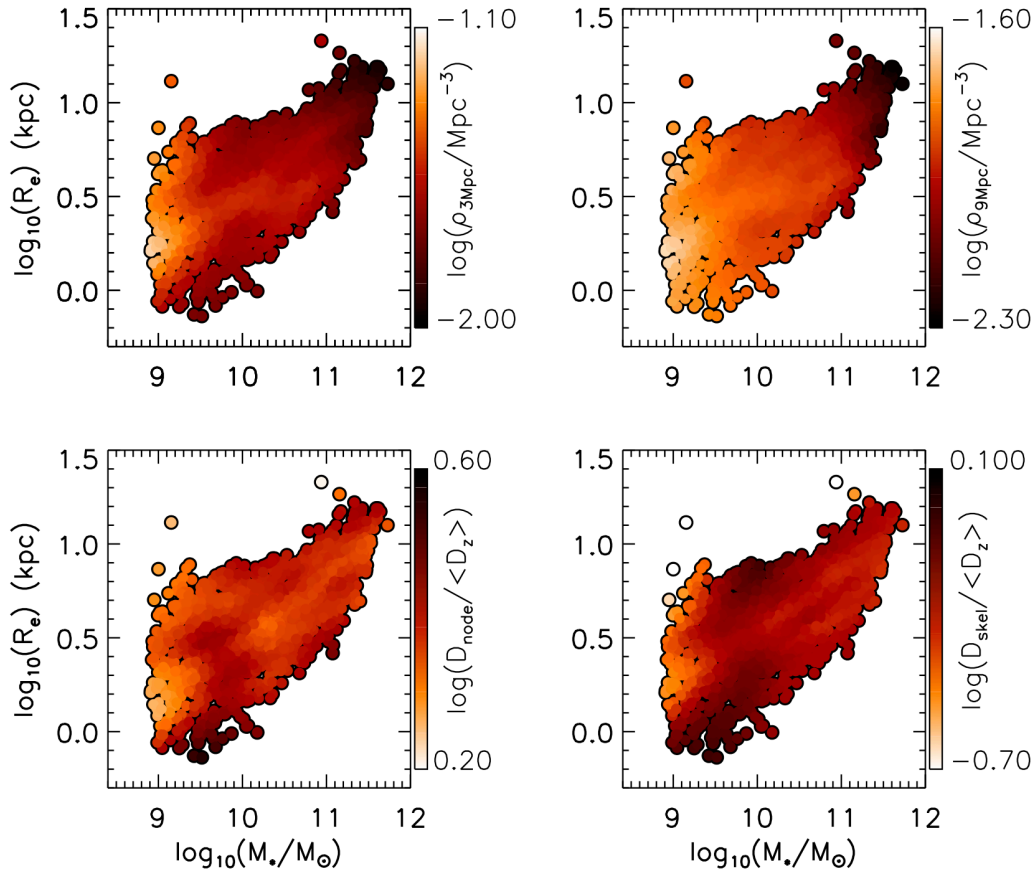


**Figure 8.** Environment measures plotted across the mass-size plane with LEOSS smoothing applied. Data points are coloured by local density calculated by a 3 Mpc (top left) or 9 Mpc (top right) Gaussian kernel, by the nearest node distance (bottom left) and by the nearest filament distance (bottom right). We invert the color scale on the bottom two panels, such that darker colours are associated with less dense environments.

model presented in Wang & Lilly (2022a), which is argued in that paper to be sufficient to reproduce the observed exponential structure of star-forming discs. Wang & Lilly (2022b) subsequently found this model to be capable of reproducing gas metallicity gradients: radially-inflowing gas continuously enriches as it travels closer to a galaxies’ centre, naturally giving rise to negative metallicity gradients. However, observational evidence of significant inward gas flows remains scarce: though Schmidt et al. (2016) reports significant inflow activity from direct HI observations, most such studies report results consistent with little activity (Wong et al. 2004; Trachternach et al. 2008; Di Teodoro & Peek 2021).

Hwang et al. (2019) employed the  $M_*$ - $\Sigma_*$ -O/H relation to identify and study regions with anomalously low gas metallicities in MaNGA galaxies; amongst other results, they found such regions to be preferentially located in galaxies’ outer parts. Luo et al. (2021) subsequently studied the N/O abundance ratios of star-forming gas and found anomalously-low metallicities to be associated with elevated N/O ratios at a given metallicity, with the greatest elevations seen at the largest radii; from simple models, they argue this to be evi-

dence for metal-poor gas inflows. Such results are consistent with the Wang & Lilly (2022b) scenario, in which metal-poor gas migrates inwards from the outer parts of a disc. More generally, these results highlight the likely importance of metal-poor inflows in understanding gas metallicity gradients, and they support a view in which inflows preferentially occur at larger radii. Such a view is entirely consistent with our findings for extended galaxies.

By contrast, more massive and more compact galaxies possess flatter gas metallicity gradients and hence display weaker metallicity-radius correlations, suggesting that other factors are relevant in shaping the metallicity distributions of these systems. One possibility is that these galaxies possess increased escape velocities due to their compactness, resulting in reduced metal outflows and a higher relative dependence on  $\Sigma_*$  (which, in this picture, serves as a proxy for the gas content). However, it can be seen from Figure 1 that  $\rho_\Sigma$  actually weakens somewhat within the most compact massive galaxies, making it worthwhile to explore additional explanations.

At a given stellar mass, compact galaxies possess earlier-

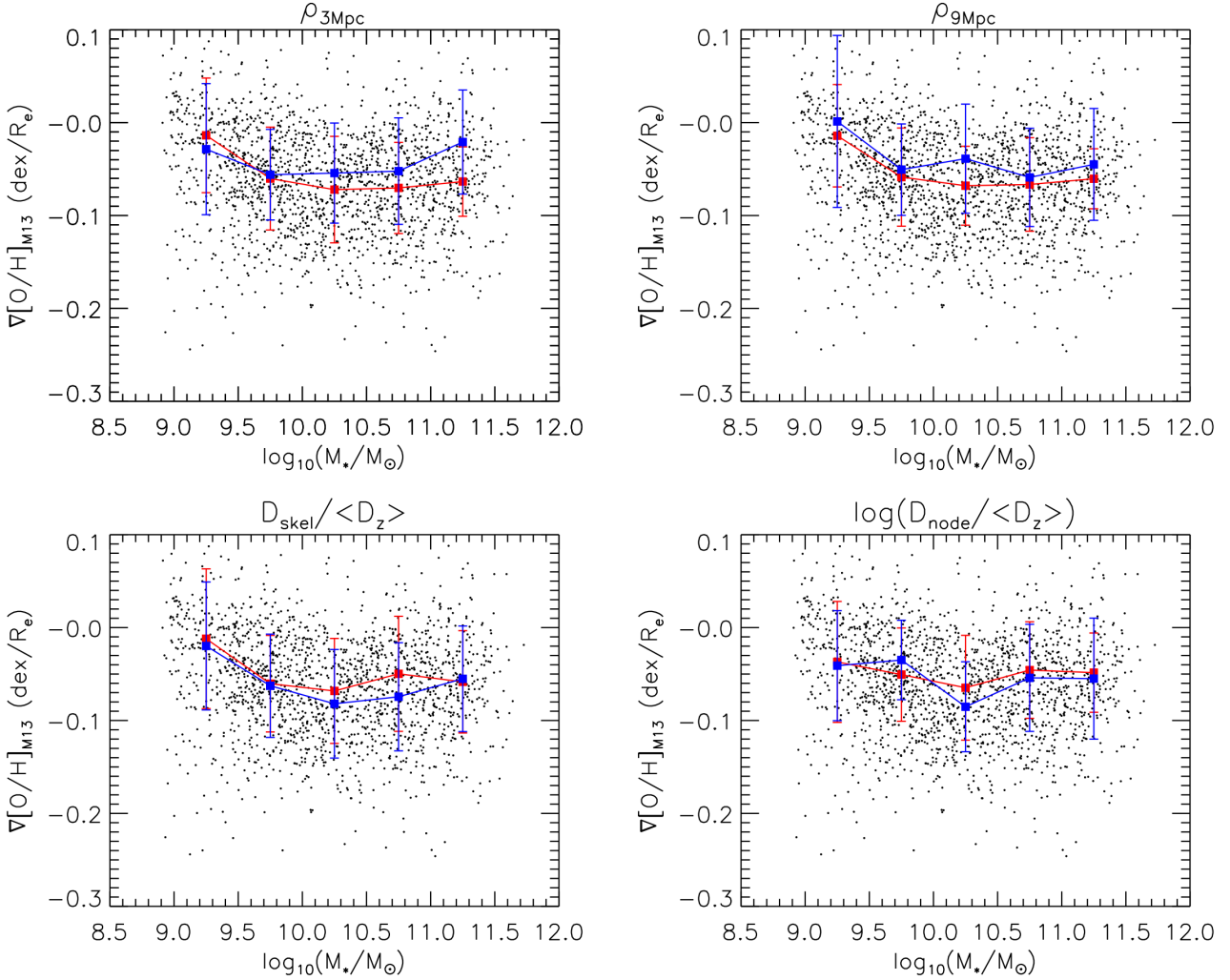


**Figure 9.** B22 gas metallicity gradient as a function of stellar mass. The blue (red) squares show the median gradients for galaxies in the top (bottom) 10 percentiles in a given environment measure, as indicated by the panel titles: local density with a 3 Mpc kernel (top left), local density with a 9 Mpc kernel, nearest filament distance (bottom left) and nearest node distance (bottom right).

type morphology than their more extended counterparts (e.g. Fernández Lorenzo et al. 2013; Boardman et al. 2021). To explore this point further, we cross-match our sample with the catalog of Simard et al. (2011) to obtain light-weighted r-band B/T values for our galaxies, employing the fits in which the bulge Sérsic index was fixed to 4. We obtain values for 2013 galaxies (94.6 % of our full sample), and we plot these with LOESS smoothing applied in Figure 10. As expected, we find very low average B/T values amongst lower mass extended galaxies, with B/T then rising for more massive and more compact galaxies. Thus, low B/T ratios appear to be associated with strong metallicity-gradient correlations and (particularly for higher-mass galaxies) with steeper gas metallicity gradients in general. In turn, higher B/T ratios are then associated with flatter gradients and a weaker metallicity-radius dependence.

Fu et al. (2013) have previously reported a significant connection between gas metallicity gradients and B/T mass ra-

tios: in both semi-analytic models and data (Moran et al. 2012), smaller B/T values are associated with steeper gas metallicity gradients. Fu et al. (2013) ascribe this to differences in galaxies’ merger histories: model galaxies with steep metallicity gradients are those which have continuously accreted gas in an undisturbed way, while model galaxies with shallow/flat gradients have experienced greater merging activity. In the Fu et al. (2013) models, mergers trigger central starbursts and grow galaxies’ bulges while also flattening metallicity gradients, with gradients then gradually steepening once smooth gas accretion resumes. Fu et al. (2013) also consider the effects of inward radial flows, but find them to have little impact on gradients. It should be noted that Yates et al. (2021) find no such B/T-gradient dependence in their own semi-analytic models, which employ a later version of the L-Galaxies code used by Fu et al. (2013); however, Yates et al. (2021) select their sample to include only disk-

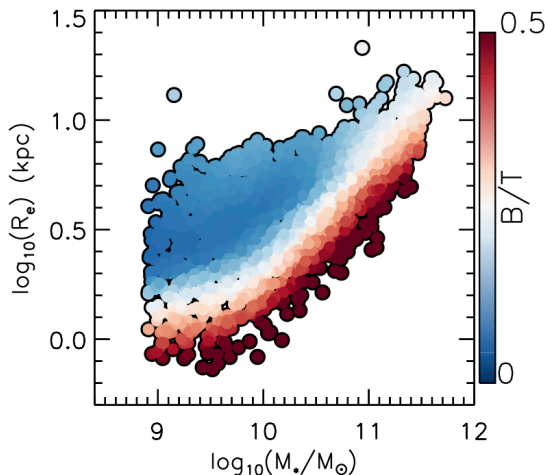


**Figure 10.** Galaxy bulge-to-total ratios from Simard et al. (2011) plotted across the mass-size plane with LOESS smoothing applied. The color scale is such that blue regions indicate dominant disc components, with red regions indicating increasingly prominent bulges.

dominated ( $B/T < 0.3$ ) galaxies, which is a possible factor in their different findings.

Concerning the impact of mergers on gas metallicity profiles, various hydrodynamical simulations have likewise found merging/interaction activity to disrupt and flatten metallicity gradients (e.g. Rupke et al. 2010; Torrey et al. 2012). Such a picture also has some observational support, with Kewley et al. (2010) reporting flatter gradients in close galaxy pairs. A connection between mergers and bulge-growth has also been reported in simulations (e.g. Hopkins et al. 2010; Sauvaget et al. 2018). Mergers have been associated in simulations with spin reorientation (Welker et al. 2014), with galaxies transitioning from parallel to perpendicular with respect to their nearest filament; a similar observational effect has been reported by Barsanti et al. (2022) between spin alignment and bulge mass (see also Kraljic et al. 2021, concerning the connection between alignment and morphology). Thus, we find it plausible that different merging histories can explain differences in metallicity gradient behaviour across the mass-size plane, particularly amongst more massive galaxies.

As has been previously noted for MaNGA galaxies, we see a flattening in gas metallicity gradients at low stellar masses. Such galaxies are metal-poorer overall than their higher-mass counterparts (e.g., Lequeux et al. 1979; Tremonti et al. 2004), and consequently can be expected to have evolved at a slower rate (Asari et al. 2007; Camps-Fariña et al. 2021, 2022). Increased metal outflows likely play a role in the flattening of low mass galaxies’ gradients (e.g. Belfiore et al. 2019b), along with wind recycling (e.g. Belfiore et al. 2017, and references therein). Stellar metallicity distributions for low-mass spirals also appear consistent with little metal-poor gas accretion, which is not the case for higher-mass spirals (Greener et al. 2021). In addition, low-mass MaNGA galaxies have been found to possess flatter gas density profiles than do higher-mass objects (Barrera-Ballesteros et al. 2022), possibly due to shallower gravitational potentials in low-mass objects. Thus,

we argue that a reduced prominence of metal-poor inflows and an increased prominence of metal outflows, along with shallower gravitational potentials more generally, are what lead to flatter gas metallicity gradients in low-mass galaxies.

A potential concern in this study is the effects of beam smearing from the MaNGA PSF, particularly for galaxies observed with 19-bundle and 37-bundle fibre-IFUs. Such galaxies have the smallest spatial extents on the sky, and Belfiore et al. (2017) have shown this to be associated with flatter calculated gas metallicity gradients in MaNGA galaxies. With this in mind, Boardman et al. (2021) considered how MaNGA gas abundance varied with both angular (in arcseconds) and physical (in kpc) galaxy size and found significant trends between gas metallicity and *physical* size at most given angular sizes; Boardman et al. (2021) thus argued that gradient trends across the mass-size plane are not a result of MaNGA PSF effects, and we likewise argue that PSF effects are not the cause of our results here. The importance of PSF effects could be minimised by cutting explicitly on angular galaxy size; however, this would bias our sample towards intrinsically larger galaxies (Wake et al. 2017) and would reduce the coverage of our sample across the mass-size plane, so we do not consider such an approach to be optimal for our purposes.

The overall interpretation we advocate is as follows. At any given mass, the most extended galaxies are those with the smoothest gas accretion histories. These galaxies form in an inside-out manner, resulting in steep metallicity gradients and large stellar discs. More compact galaxies have experienced more significant merging activity, by contrast, and so possess more significant bulges along with flatter metallicity gradients due to disruption of previously-established metallicity profiles. Finally, the least massive galaxies are more susceptible to significant metal outflows while also experiencing less metal-poor inflow (as evidenced by their abundant low-metallicity stars), resulting in flatter gradients overall.

## 5 SUMMARY AND CONCLUSION

In this paper, we have employed MaNGA data to study local gaseous and stellar metallicity as functions of stellar mass surface density and of galactocentric radius. We considered star-forming spaxels across each individual sample galaxy in turn, while also considering spaxels across galaxies grouped according to their position within the mass-size plane.

Amongst lower mass extended galaxies, we found spaxels’ gas metallicity to correlate more strongly with galactocentric radius than with density. The local relations considered in B22 – which do not include radius – are not able to replicate this finding. Thus, we argue that radius is an important parameter in its own right for understanding gas metallicities on local scales: metallicities are strongly related to the radius, or else are related to one or more parameters strongly correlated with the radius. We argued our findings to be consistent with a view in which extended galaxies experienced comparatively smooth gas accretion histories, with metal-poor inflows and metal outflows both preferentially affecting the galaxies’ outer parts; this, along with the inside-out evolution of galaxies, naturally gives rise to negative metallicity gradients. Our results here could also be explained by the presence of significant inward radial flows, as formalised for instance by the ‘modified accretion disc’ framework (Wang & Lilly 2022a,b),

but observational support for this view remains limited at present.

More compact higher-mass galaxies, meanwhile, possess a reduced correlation between gas metallicity and radius – something that is to be expected given their relatively flattened gradients. In this case, stellar density provides a stronger correlation than radius once the effect of uncertainties are considered. This difference is associated with earlier-type morphologies – that is, more prominent bulges – and we argue this to reflect the impact of different merger histories for galaxies of different morphologies.

We also investigated the impact of environment, including position within the Cosmic Web, finding only a limited connection between gas metallicity gradients and local environment. We also detected no significant connections between environment and galaxy size. We therefore argued that environment variations are *not* sufficient to explain the findings described above.

Various potential extensions to this work remain. A machine learning approach (e.g. Bluck et al. 2019, 2020) that includes spaxel radii along with other local parameters would allow for a more thorough investigation of local relations. Chemical evolution modelling for different classes of galaxy across the mass-size plane could also prove fruitful.

## ACKNOWLEDGEMENTS

For the purpose of open access, the author has applied a Creative Commons Attribution (CC BY) licence to any Author Accepted Manuscript version arising. The support and resources from the Center for High Performance Computing at the University of Utah are gratefully acknowledged. NFB and VW acknowledge STFC grant ST/V000861/1.

Funding for the Sloan Digital Sky Survey IV has been provided by the Alfred P. Sloan Foundation, the U.S. Department of Energy Office of Science, and the Participating Institutions. SDSS-IV acknowledges support and resources from the Center for High-Performance Computing at the University of Utah. The SDSS web site is [www.sdss.org](http://www.sdss.org). J.B-B thanks IA-100420 (DGAPA-PAPIIT, UNAM) and CONACYT grant CF19-39578 support. RR thanks Conselho Nacional de Desenvolvimento Científico e Tecnológico (CNPq, Proj. 311223/2020-6, 304927/2017-1 and 400352/2016-8), Fundação de amparo à pesquisa do Rio Grande do Sul (FAPERGS, Proj. 16/2551-0000251-7 and 19/1750-2), Coordenação de Aperfeiçoamento de Pessoal de Nível Superior (CAPES, Proj. 0001). RAR acknowledges financial support from Conselho Nacional de Desenvolvimento Científico e Tecnológico (302280/2019-7).

SDSS-IV is managed by the Astrophysical Research Consortium for the Participating Institutions of the SDSS Collaboration including the Brazilian Participation Group, the Carnegie Institution for Science, Carnegie Mellon University, the Chilean Participation Group, the French Participation Group, Harvard-Smithsonian Center for Astrophysics, Instituto de Astrofísica de Canarias, The Johns Hopkins University, Kavli Institute for the Physics and Mathematics of the Universe (IPMU) / University of Tokyo, Lawrence Berkeley National Laboratory, Leibniz Institut für Astrophysik Potsdam (AIP), Max-Planck-Institut für Astronomie (MPIA Heidelberg), Max-Planck-Institut für Astro-

physik (MPA Garching), Max-Planck-Institut für Extraterrestrische Physik (MPE), National Astronomical Observatories of China, New Mexico State University, New York University, University of Notre Dame, Observatório Nacional / MCTI, The Ohio State University, Pennsylvania State University, Shanghai Astronomical Observatory, United Kingdom Participation Group, Universidad Nacional Autónoma de México, University of Arizona, University of Colorado Boulder, University of Oxford, University of Portsmouth, University of Utah, University of Virginia, University of Washington, University of Wisconsin, Vanderbilt University, and Yale University.

## DATA AVAILABILITY

All non-MaNGA data used here are publically available, as are all MaNGA data as of SDSS DR17.

## REFERENCES

- Abdurro'uf et al., 2022, *ApJS*, 259, 35  
 Asari N. V., Cid Fernandes R., Stasińska G., Torres-Papaqui J. P., Mateus A., Sodr e L., Schoenell W., Gomes J. M., 2007, *MNRAS*, 381, 263  
 Baldwin J. A., Phillips M. M., Terlevich R., 1981, *PASP*, 93, 5  
 Barrera-Ballesteros J. K., et al., 2016, *MNRAS*, 463, 2513  
 Barrera-Ballesteros J. K., et al., 2018, *ApJ*, 852, 74  
 Barrera-Ballesteros J. K., et al., 2022, arXiv e-prints, p. arXiv:2206.07058  
 Barsanti S., et al., 2022, arXiv e-prints, p. arXiv:2208.10767  
 Belfiore F., et al., 2017, *MNRAS*, 469, 151  
 Belfiore F., et al., 2019a, *AJ*, 158, 160  
 Belfiore F., Vincenzo F., Maiolino R., Matteucci F., 2019b, *MNRAS*, 487, 456  
 Blanton M. R., Kazin E., Muna D., Weaver B. A., Price-Whelan A., 2011, *AJ*, 142, 31  
 Bluck A. F. L., et al., 2019, *MNRAS*, 485, 666  
 Bluck A. F. L., Maiolino R., S anchez S. F., Ellison S. L., Thorp M. D., Piotrowska J. M., Teimoorinia H., Bundy K. A., 2020, *MNRAS*, 492, 96  
 Boardman N. F., Zasowski G., Newman J. A., Sanchez S. F., Schaefer A., Lian J., Bizyaev D., Drory N., 2021, *MNRAS*, 501, 948  
 Boardman N., et al., 2022, *MNRAS*, 514, 2298  
 Bruzual A. G., 1983, *ApJ*, 273, 105  
 Bundy K., et al., 2015, *ApJ*, 798, 7  
 Camps-Fari a A., Sanchez S. F., Lacerda E. A. D., Carigi L., Garc a-Benito R., Mast D., Galbany L., 2021, *MNRAS*, 504, 3478  
 Camps-Fari a A., et al., 2022, *ApJ*, 933, 44  
 Carton D., et al., 2015, *MNRAS*, 451, 210  
 Carton D., et al., 2018, *MNRAS*, 478, 4293  
 Cebri an M., Trujillo I., 2014, *MNRAS*, 444, 682  
 Cherinka B., et al., 2019, *AJ*, 158, 74  
 Cleveland W. S., Devlin S. J., 1988, *Journal of the American Statistical Association*, 83, 596  
 Croom S. M., et al., 2012, *MNRAS*, 421, 872  
 Di Teodoro E. M., Peek J. E. G., 2021, *ApJ*, 923, 220  
 Drory N., et al., 2015, *AJ*, 149, 77  
 Duckworth C., Tojeiro R., Kraljic K., Sgr o M. A., Wild V., Weijmans A.-M., Lacerna I., Drory N., 2019, *MNRAS*, 483, 172  
 Fern andez Lorenzo M., Sulentic J., Verdes-Montenegro L., Argudo-Fern andez M., 2013, *MNRAS*, 434, 325  
 Franchetto A., et al., 2021, *ApJ*, 923, 28  
 Fu J., et al., 2013, *MNRAS*, 434, 1531

- Gao Y., et al., 2018, *ApJ*, 868, 89
- García-Benito R., et al., 2017, *A&A*, 608, A27
- Greener M. J., Merrifield M., Aragón-Salamanca A., Peterken T., Andrews B., Lane R. R., 2021, *MNRAS*, 502, L95
- Gunn J. E., et al., 2006, *AJ*, 131, 2332
- Hopkins P. F., et al., 2010, *ApJ*, 715, 202
- Hwang H.-C., et al., 2019, *ApJ*, 872, 144
- Kewley L. J., Ellison S. L., 2008, *ApJ*, 681, 1183
- Kewley L. J., Rupke D., Zahid H. J., Geller M. J., Barton E. J., 2010, *ApJ*, 721, L48
- Kraljic K., Duckworth C., Tojeiro R., Alam S., Bizyaev D., Weijmans A.-M., Boardman N. F., Lane R. R., 2021, *MNRAS*, 504, 4626
- Kroupa P., 2001, *MNRAS*, 322, 231
- Kroupa P., Weidner C., 2003, *ApJ*, 598, 1076
- Kuchner U., Ziegler B., Verdugo M., Bamford S., Häußler B., 2017, *A&A*, 604, A54
- Lara-López M. A., et al., 2022, *A&A*, 660, A105
- Law D. R., et al., 2015, *AJ*, 150, 19
- Law D. R., et al., 2016, *AJ*, 152, 83
- Lequeux J., Peimbert M., Rayo J. F., Serrano A., Torres-Peimbert S., 1979, *A&A*, 500, 145
- Li H., et al., 2018, *MNRAS*, 476, 1765
- Lian J., Thomas D., Li C., Zheng Z., Maraston C., Bizyaev D., Lane R. R., Yan R., 2019, *MNRAS*, 489, 1436
- Lilly S. J., Carollo C. M., Pipino A., Renzini A., Peng Y., 2013, *ApJ*, 772, 119
- Luo Y., et al., 2021, *ApJ*, 908, 183
- Marino R. A., et al., 2013, *A&A*, 559, A114
- Mingozzi M., et al., 2020, *A&A*, 636, A42
- Moran S. M., et al., 2012, *ApJ*, 745, 66
- Neumann J., et al., 2021, *MNRAS*, 508, 4844
- Pilyugin L. S., Grebel E. K., 2016, *MNRAS*, 457, 3678
- Rosales-Ortega F. F., Sánchez S. F., Iglesias-Páramo J., Díaz A. I., Vílchez J. M., Bland-Hawthorn J., Husemann B., Mast D., 2012, *ApJ*, 756, L31
- Rupke D. S. N., Kewley L. J., Barnes J. E., 2010, *ApJ*, 710, L156
- Salim S., et al., 2016, *ApJS*, 227, 2
- Salim S., Boquien M., Lee J. C., 2018, *ApJ*, 859, 11
- Sánchez S. F., 2020, *ARA&A*, 58, 99
- Sánchez-Menguiano L., et al., 2018, *A&A*, 609, A119
- Sánchez-Menguiano L., Sánchez Almeida J., Muñoz-Tuñón C., Sánchez S. F., Filho M., Hwang H.-C., Drory N., 2019, *ApJ*, 882, 9
- Sánchez S. F., et al., 2012a, *A&A*, 538, A8
- Sánchez S. F., et al., 2012b, *A&A*, 546, A2
- Sánchez S. F., et al., 2013, *A&A*, 554, A58
- Sánchez S. F., et al., 2014, *A&A*, 563, A49
- Sánchez S. F., et al., 2016a, *Rev. Mex. Astron. Astrofis.*, 52, 21
- Sánchez S. F., et al., 2016b, *Rev. Mex. Astron. Astrofis.*, 52, 171
- Sánchez S. F., et al., 2018, *Rev. Mex. Astron. Astrofis.*, 54, 217
- Sánchez S. F., Walcher C. J., Lopez-Cobá C., Barrera-Ballesteros J. K., Mejía-Narváez A., Espinosa-Ponce C., Camps-Fariña A., 2021, *Rev. Mex. Astron. Astrofis.*, 57, 3
- Sauvaget T., Hammer F., Puech M., Yang Y. B., Flores H., Rodrigo M., 2018, *MNRAS*, 473, 2521
- Schaefer A. L., et al., 2019, *ApJ*, 884, 156
- Schaefer A. L., Tremonti C., Belfiore F., Pace Z., Bershadsky M. A., Andrews B. H., Drory N., 2020, *ApJ*, 890, L3
- Schmidt M., 1963, *ApJ*, 137, 758
- Schmidt T. M., Bigiel F., Klessen R. S., de Blok W. J. G., 2016, *MNRAS*, 457, 2642
- Simard L., Mendel J. T., Patton D. R., Ellison S. L., McConnachie A. W., 2011, *ApJS*, 196, 11
- Smee S. A., et al., 2013, *AJ*, 146, 32
- Tempel E., et al., 2014, *A&A*, 566, A1
- Torrey P., Cox T. J., Kewley L., Hernquist L., 2012, *ApJ*, 746, 108
- Trachternach C., de Blok W. J. G., Walter F., Brinks E., Kennicutt R. C. J., 2008, *AJ*, 136, 2720
- Trapp C. W., et al., 2022, *MNRAS*, 509, 4149
- Tremonti C. A., et al., 2004, *ApJ*, 613, 898
- Wake D. A., et al., 2017, *AJ*, 154, 86
- Wang E., Lilly S. J., 2022a, *ApJ*, 927, 217
- Wang E., Lilly S. J., 2022b, *ApJ*, 929, 95
- Welker C., Devriendt J., Dubois Y., Pichon C., Peirani S., 2014, *MNRAS*, 445, L46
- Westfall K. B., et al., 2019, *AJ*, 158, 231
- Wong T., Blitz L., Bosma A., 2004, *ApJ*, 605, 183
- Yan R., et al., 2016a, *AJ*, 151, 8
- Yan R., et al., 2016b, *AJ*, 152, 197
- Yates R. M., Henriques B. M. B., Fu J., Kauffmann G., Thomas P. A., Guo Q., White S. D. M., Schady P., 2021, *MNRAS*, 503, 4474
- Zhu G. B., Barrera-Ballesteros J. K., Heckman T. M., Zakamska N. L., Sánchez S. F., Yan R., Brinkmann J., 2017, *MNRAS*, 468, 4494

## APPENDIX A: RESULTS WITH R2 CALIBRATOR

Thus far, we have focussed on gas metallicity results from the O3N2 calibrator of Marino et al. (2013). This calibrator has the advantage of simplicity, due to it being essentially unaffected by dust attenuation. However, different calibrators can lead to notably different outcomes in terms of gas metallicities and gas metallicity gradients (e.g. Kewley & Ellison 2008; Schaefer et al. 2020), and the O3N2 calibrator implicitly assumes a fixed N/O-O/H relation which, in practice, will not be true for all spaxels (e.g. Luo et al. 2021). As such, we briefly present results from the R2 calibrator of Pilyugin & Grebel (hereafter P16 2016), as was done in Appendix B of B22.

Similarly to the M13 calibrator, the P16 R2 calibrator was determined from observational data; however, it employs the [OII] $\lambda$ 3737,3729 doublet in addition to the lines within the O3N2 indicator, making the R2 calibrator more resistant to biases from N/O variations. The R2 calibrator employs the full [OIII] and [NII] doublets, so we assume a 1/3 ratio between the dominant and subdominant lines of these doublets. We employ the same spaxel/galaxy sample presented in the main paper text.

We present in Figure A1 gas metallicity gradients,  $\rho_{\Sigma}$  and  $\rho_R$  values across the mass-size plane. These were calculated in an identical manner to what was described in the main paper text, but with P16 metallicities instead of M13 metallicities. We then present in Figure A2 a comparison between  $|\rho_{\Sigma}|$  and  $|\rho_R|$  and between  $|\rho_{\Sigma}|$  and  $|\rho_{R,perturbed}|$ , with all values calculated in the same way as before. Finally, we present in Figure A3 the behaviour of B22 ‘SFH models’ as derived from the P16 calibrator.

The correlations are found to be a little weaker here than was found from the M13 calibrator; this is unsurprising, as B22 previously noted a larger scatter in gas metallicity relations when the P16 R2 calibrator was applied. Nonetheless, we obtain the same broad results that were presented and discussed in the main paper text:  $\rho_{\Sigma}$  and  $\rho_R$  trend similarly to the gradients across the mass-size plane, as is to be expected, with  $|\rho_R|$  greater than  $|\rho_{\Sigma}|$  for less massive extended galaxies. We further find that the SFH models remain unable to replicate this behaviour, predicting stronger metallicity correlations with  $\Sigma_*$  than with radius. Thus, we find that the

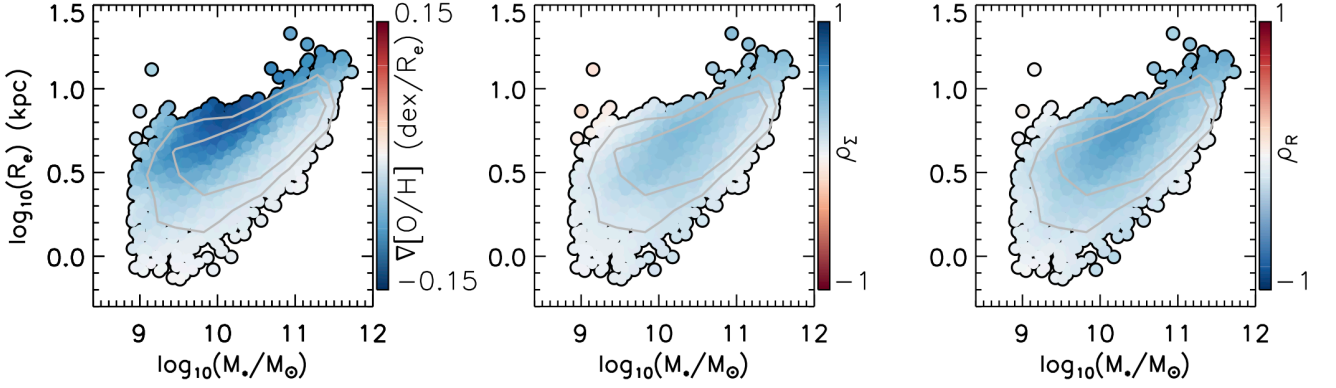


**Figure A1.** Effective radius plotted against galaxy stellar mass, with data points coloured by the radial gas metallicity gradients (left) and by the Spearman correlation coefficients between  $\Sigma_*$  and metallicity (middle) and between radius and metallicity (right); the gas metallicity here is determined from the P16 calibrator. We apply LOESS smoothing in all panels. The middle panel uses a reversed colour scale; thus, blue regions correspond to negative gradients, positive  $\Sigma_*$ -metallicity correlations and negative radius-metallicity correlations. The contours enclose  $\sim 50\%$  and  $\sim 80\%$  of galaxies.

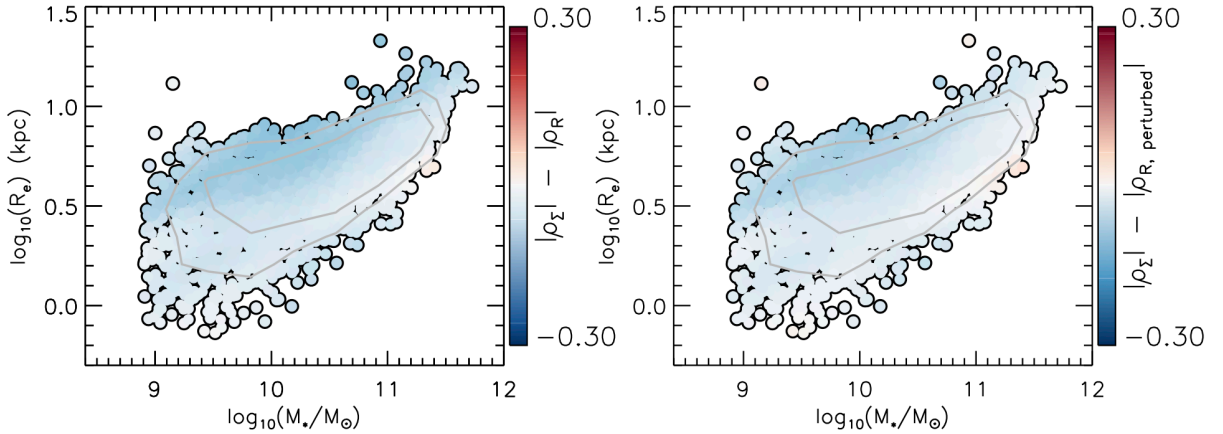


**Figure A2.** Difference in magnitudes of the Spearman correlation coefficient between gas metallicity and stellar density,  $|\rho_\Sigma|$ , and the coefficient between gas metallicity and galactocentric radius before ( $|\rho_R|$ ; left panel) and after ( $|\rho_{R,perturbed}|$ ; right panel) perturbing spaxel radii. Each datapoint represents one galaxy, and LOESS smoothing is applied; blue regions indicate where metallicity is more strongly correlated with radius, while red regions indicate a stronger correlation with density. The contours enclose  $\sim 50\%$  and  $\sim 80\%$  of galaxies.

main results from this paper are *not* simply due to the use of the M13 calibrator.

## APPENDIX B: RELATION BETWEEN GAS METALLICITY GRADIENTS AND CORRELATION COEFFICIENTS

We now explore in more depth how the gas metallicity gradients relate to  $\rho_R$  and  $\rho_\Sigma$ , focussing specifically on the M13 calibrator. In Figure B1, we plot both  $\rho_R$  and  $\rho_\Sigma$  against the radial metallicity gradient; as was already apparent, steeper gradients are associated more positive  $\rho_\Sigma$  values and more negative  $\rho_R$  values.

Next, we consider how metallicity gradients vary with  $\rho_\Sigma$  and  $\rho_R$  at different locations in the mass-size parameter space. For this, we employ the six mass-size subsamples described in Section 3.2. We plot in Figure B2 the gas metallicity gradients against  $\rho_\Sigma$  for each of the subsamples, while in Figure B3 we compare the metallicity gradients and  $\rho_R$  in the same manner.

For both the sample as a whole and for the mass-size subsamples, it is apparent that the gradient correlates tightly with  $\rho_\Sigma$  and especially with  $\rho_R$ . This is by construction:  $\Sigma_*$  declines with radius, meaning that steeper gradients can be immediately expected to yield tighter metallicity correlations with both  $\Sigma_*$  and radius.

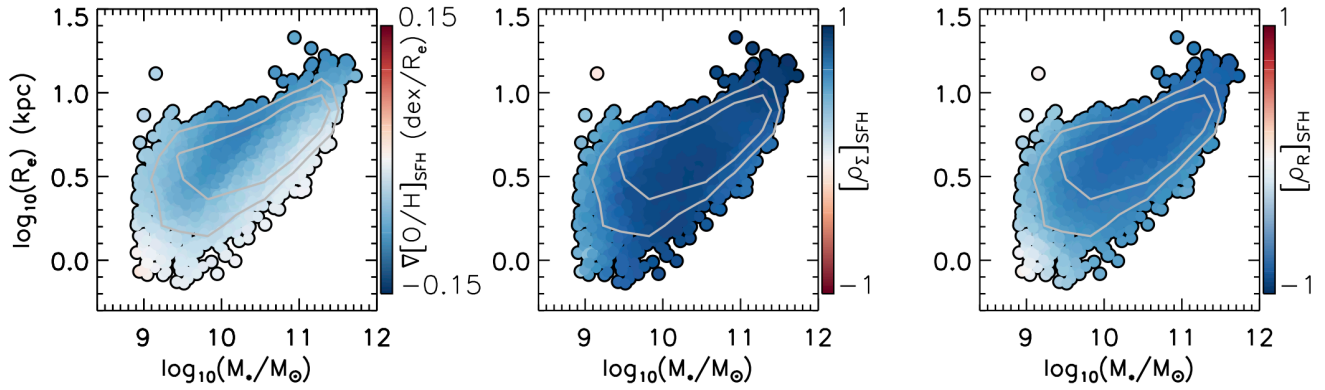


**Figure A3.** Effective radius, plotted against galaxy stellar mass, with data points coloured by the B22 ‘SFH model’ metallicity gradients (left) and by the Spearman correlation coefficients between  $\Sigma_*$  and model metallicity ( $[\rho_\Sigma]_{SFH}$ , middle) and between radius and model metallicity (right). The model metallicities were built using the P16 R2 indicator in this case. We apply LOESS smoothing in all panels, and the middle panel uses a reversed colour scale. The contours enclose  $\sim 50\%$  and  $\sim 80\%$  of galaxies. We find that the SFH models do *not* reproduce the trends shown in Figures 1 and 2 for observed gas metallicities: while individual parameters behave similarly across the mass-size plane, we find local metallicities to be correlated more strongly with stellar density than with radius in most cases.

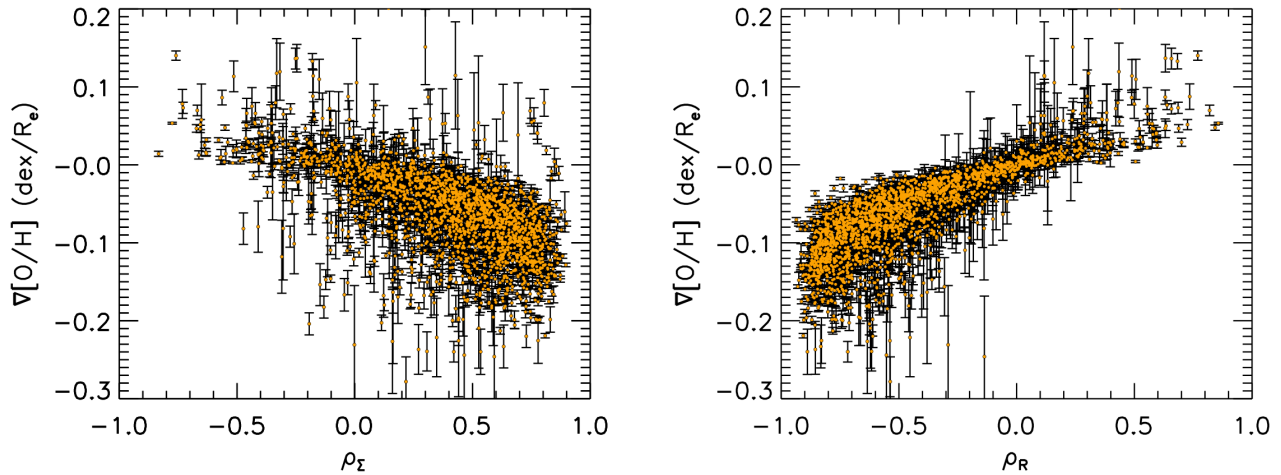


**Figure B1.** Radial gas metallicity gradients plotted against  $\rho_\Sigma$  (left) and  $\rho_R$  (right), with gradients obtained using the M13 calibrator. A small number of anomalous gradient values are not shown for presentational purposes.

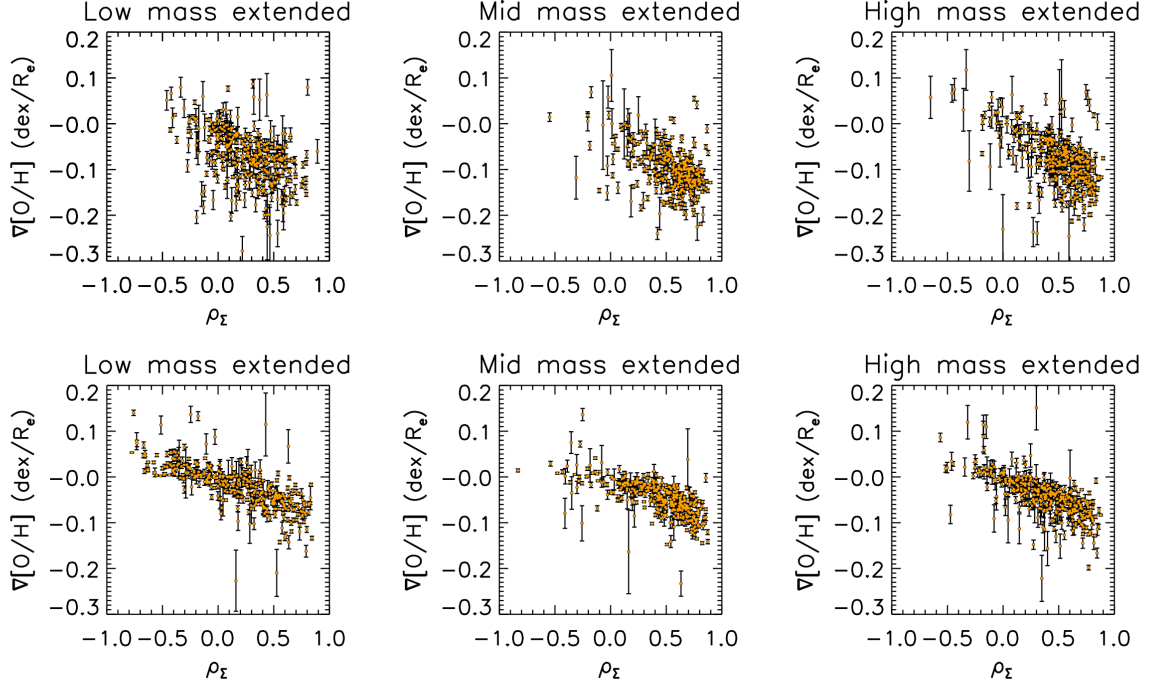


Figure B2. Radial gas metallicity gradients plotted against  $\rho_z$  for the six mass-size bins first described in Section 3.2.

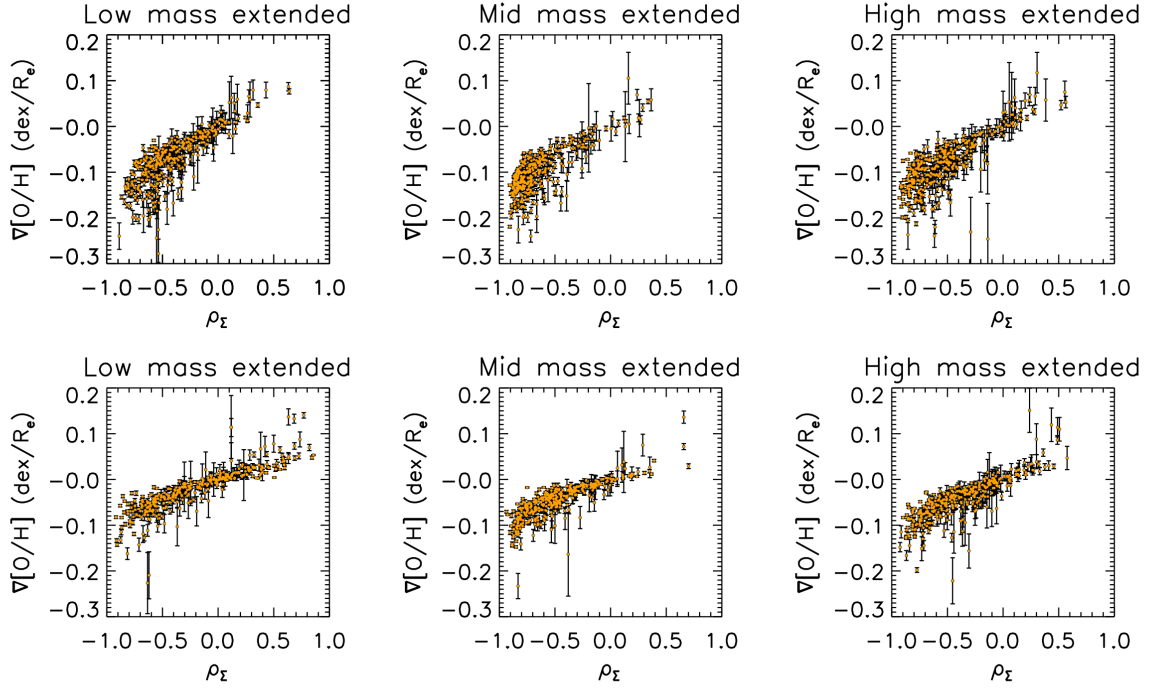


Figure B3. Radial gas metallicity gradients plotted against  $\rho_R$  for the six mass-size bins first described in Section 3.2.